Polarity inversions within AlN films on sapphire exploiting silicon and oxygen diffusion during high temperature annealing

Valeria Bonito Oliva, Sylvia Hagedorn, Eric Robin, Holm Kirmse, Jean-Luc Rouviere, Hanako Okuno, Benjamin Damilano, Adrien Michon, Thilo Remmele, Tobias Schulz, et al.

Polarity inversions within AlN films on sapphire exploiting silicon and oxygen diffusion during high temperature annealing

V. Bonito Oliva[1,2,a*], S. Hagedorn[3], E. Robin[4], H. Kirmse[5], J. L. Rouviere[4], H. Okuno[4], B. Damilano[2], T. Remmele[1], A. Michon[2], T. Schulz[1], H. Amari[1], M. Albrecht[1], and P. Vennéguès[2]

[1]*Leibniz-Institut für Kristallzüchtung, Max-Born Straße 2, 12489 Berlin, Germany*
[2]*Université Côte d'Azur, CRHEA-CNRS, rue B. Grégory, 06560 Valbonne, France*
[3]*Ferdinand-Braun-Institut gGmbH Leibniz-Institut für Höchstfrequenztechnik, Gustav-Kirchhoff-Str. 4, 12489 Berlin, Germany*
[4]*CEA-Grenoble INAC/SP2M/LEMMA, 17 rue des Martyrs, 38054 Grenoble Cedex 9, France*
[5]*Humboldt-Universität zu Berlin, Institut für Physik, Newton Straße 15, 12489 Berlin, Germany*
*email: valeria.bonitooliva@gmail.com

[a)]**now:** *Photonics Research Group, Department of Information Technology (INTEC), Ghent University – imec, Technologiepark-Zwijnaarde 126, 9052 Ghent, Belgium*

Abstract

The polarity of III-nitride materials plays a crucial role in determining their physical properties and behavior. In this study, we investigate the formation and characteristics of elongated polarity inversion domains (IDs) in epitaxial aluminum nitride (AlN) layers grown on sapphire substrates during high temperature annealing. By employing various characterization techniques, we explore the chemical composition and atomic structure of the AlN epilayers. The domains exhibit distinct boundaries, indicating polarity inversions from aluminum Al-polar to N-polar and back to Al-polar. Significantly, we find that this inversion of polarity occurs post-growth during the annealing process, representing a novel finding of this study. The inclusion of silicon (Si) and oxygen (O) impurities during annealing proves crucial for the formation and stabilization of these domains. Chemical composition analysis demonstrates enrichments of Si and O at the boundaries of the domains, accompanied by reductions in Al and N concentrations. Using high-resolution transmission electron microscopy, we gain insights into the atomic structure of the IDs. The boundaries of the domains show an abrupt transition of polarity from Al-polar to N-polar, while convex boundaries exhibit a polarity reversal back to Al-polar. Our findings highlight the role of

impurities and vacancies in the formation of IDs. Overall, this study provides significant insights into the post-growth inversion of polarity occurring during annealing in epitaxial AlN layers. The identification of IDs and the analysis of their characteristics contribute to a deeper understanding of polarity control and engineering in III-nitride materials, offering valuable implications for the design of electronic and optoelectronic devices based on polarity manipulation.

Introduction

The physical properties and behavior of III-nitride materials are significantly influenced by the polarity of their crystalline structures, which can be N-polar or metal-polar [1-5]. The emergence of domains with different polarities has implications for electronic and optoelectronic devices, offering intriguing possibilities for device designs based on polarity engineering [6-7]. However, achieving polarity control in compound semiconductors along the polar axes is a challenging task [8]. Significant advancements have been made in the growth of III-nitrides on sapphire substrates and various approaches for polarity control during growth have been developed, often relying on the implementation of buffer layers between polar layers and nonpolar substrates [9-12].

In the case of GaN, successful conversion from metal-polarity to N-polarity has been demonstrated through exposure to magnesium (Mg) of the growth surface [13-16], although achieving the opposite polarity inversion has not been achieved using this method.

For AlN, metal-polar films are obtained during metalorganic vapor phase deposition (MOVPE) through nitridation of the sapphire substrate and deposition of a low-temperature buffer layer [9-10] [17-18]. Notably, further investigations have revealed that the formation of $Al_xO_yN_z$ during nitridation is crucial for polarity switching from N-polar to Al-polar in epitaxial AlN on sapphire [19-21]. Regarding the opposite polarity inversion from metal-polar to N-polar, the introduction of specific elements during the deposition process of AlN has proven

to be an effective method. In fact, oxygen [22], germanium [23] or silicon [24] additions during the film growth promote the formation of point defects, particularly vacancies. These defects compensate for charge differences and contribute to the overall polarity inversion process. The presence of vacancies and the formation of defect clusters, along with decreased crystallinity, have been demonstrated to promote the formation of inversion domain boundaries (IDBs) in AlN thin films, ultimately leading to polarity inversion [24].

Interestingly, impurities have also been reported to influence the formation of closed inversion domains in various III-nitride materials. For instance, in epitaxial GaN, the introduction of high Mg-doping during MOVPE growth has been associated with the formation of pyramidal-shaped defects, representing domains with reversed polarity compared to the surrounding material [15][25-26], while other studies have shown the presence of extended two-dimensional defects in AlN containing O. Two different morphologies of these extended defects have been observed: a planar-variant on the basal plane {0001} of AlN [27-28] and a curved-variant [29]. These defects, identified as inversion domain boundaries (IDBs), have been linked to non-stoichiometry in the AlN, suggesting a correlation with the presence of O in both the planar [28] and the curved IDB [29]. These two distinct morphologies can occur separately or combine to form complex defects (i.e., closed IDs). Notably, Westwood et al. observed the formation of closed IDs in polycrystalline AlN powders containing O [29]. Our study represents the first report of closed IDs in epitaxial AlN, providing further insights into the nature and characteristics of these defects. Moreover, we demonstrate that these closed IDs appear after growth within the AlN epilayer following high-temperature annealing and they are originated by the inclusion of silicon and oxygen. This finding supports the notion that impurities and vacancies play a key role in their formation [24].

Experimental methods

Our study is based on the analysis of epitaxial AlN grown by metal-organic vapor phase epitaxy (MOVPE) on c-plane sapphire substrate with an off-angle towards the m-axis of 0.2°. The sapphire substrate is annealed under H_2 for 10 min at 1100°C. Then, the temperature is decreased to 830°C for the deposition of a thin Al layer (trimethylaluminum flow of 28 sccm for 7s) and the growth of an AlN buffer layer (trimethylaluminum flow of 20 sccm, and NH_3 flow of 160 sccm for 10 s) [30]. Finally, a 1.1 µm-thick AlN layer is grown at 1140°C at a growth rate of 0.8 µm/h (trimethylaluminum flow of 78 sccm and NH_3 flow of 50 sccm). Epitaxial growth is performed at a pressure of 100 mbar. A 200 nm thick layer of amorphous SiN is deposited on the surface of the AlN epi-layer using reactive sputtering deposition. One piece of the sample is kept as a reference, while other two pieces (with an area of ~1cm x 1cm) are annealed face to face in a LORA HTMReetz furnace [31] at 1700 °C for 1 hour (not considering the heating up and cooling down time) in N_2 environment at 1 atm.

The same face to face annealing process and configuration have already been applied by our group to:

- a similar AlN layer on c-plane sapphire substrate, with no top SiN amorphous layer [32];
- a bulk AlN sample grown by Physical Vapor Transport via spontaneous nucleation [33-35] and sliced into {0001} wafers. Prior to annealing, reactive sputtering has also been used to deposit an amorphous SiN 200 nm thick [36].

The present results are compared to the results obtained with those previous samples. A sketch of the annealing configurations for the different samples is shown in fig.1.

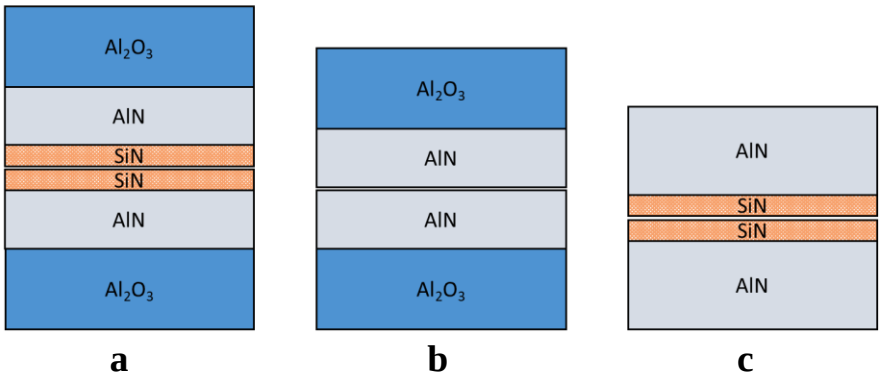

Figure 1: Face to face annealing configurations for **a)** epitaxial AlN with 200 nm of SiN deposited via reactive sputtering; **b)** epitaxial AlN on sapphire; **c)** bulk AlN with 200 nm SiN layer deposited via reactive sputtering.

In the following, we study chemical composition and atomic structure of the AlN layer before and after annealing at high temperature by secondary ion mass spectroscopy (SIMS) and (scanning) transmission electron microscopy ((S)TEM). SIMS is performed to obtain the depth profiles of silicon (Si) and oxygen (O) concentrations in AlN, using a Cameca IMS 4f-E6 with Cs^+ ions (14.5 keV acceleration) and a vertical resolution of 1 nm. To reduce the charging effect of the semi insulating AlN layer during the measurements, a thin layer (few nanometers) of gold was preliminary sputtered on the surface of the samples.

Cross-sectional samples for (S)TEM observations are prepared mainly along $AlN_{<11\text{-}20>}$ lattice direction using two different preparation methods:

- mechanical polishing with diamond foils and final thinning by Argon ion milling in a Gatan Precision Ion Polishing System (PIPS) with acceleration voltages between 4.0 and 0.2 kV and angles between 4° and 9°.
- focused ion beam (FIB) using a FEI Nova 600 Dual-beam FIB-SEM. After depositing a protective Pt capping layer, trenches were etched down to the substrate using 30 and then 20 keV Ga-ions with ion-beam currents varying from 7 nA to 50 pA.

Energy dispersive X-ray spectroscopy (EDXS) is performed in STEM mode either in a JEOL TEM/STEM 2200FS fitted with a 30 mm^2 Bruker silicon drift detector or in a probe corrected TITAN THEMIS equipped with a Bruker EDX

system consisting of four silicon drift detectors. Both TEMs are operated at 200kV.

High resolution transmission electron microscopy (HRTEM) and STEM investigations are performed in order to study the atomic structure of the AlN epilayer. HAADF-STEM images are obtained with the TITAN THEMIS microscope. In HAADF-STEM images, atomic columns appear bright and the contrast is highly sensitive to variations in the atomic number of the columns [1] [37]. Lower intensity indicates either a lower atomic number or a reduced number of atoms caused by the presence of vacancies [41]. It follows that, in AlN, aluminum (Al) columns are brighter than nitrogen (N) columns. Phase contrast HRTEM images are obtained with a FEI Titan 80-300 TEM operated at 300 keV with corrector for spherical aberrations (C_s) of the objective lens. By adjusting the imaging conditions to a slightly negative value of the spherical aberration Cs = -12 µm and a positive defocus of ~5 nm, it is possible to obtain bright atom contrast and investigate the lattice polarity of AlN [38-41].

Results

Fig. 2a and 2b show the SIMS depth profiles of Si and O, respectively, and compare the impurities concentrations before and after annealing.

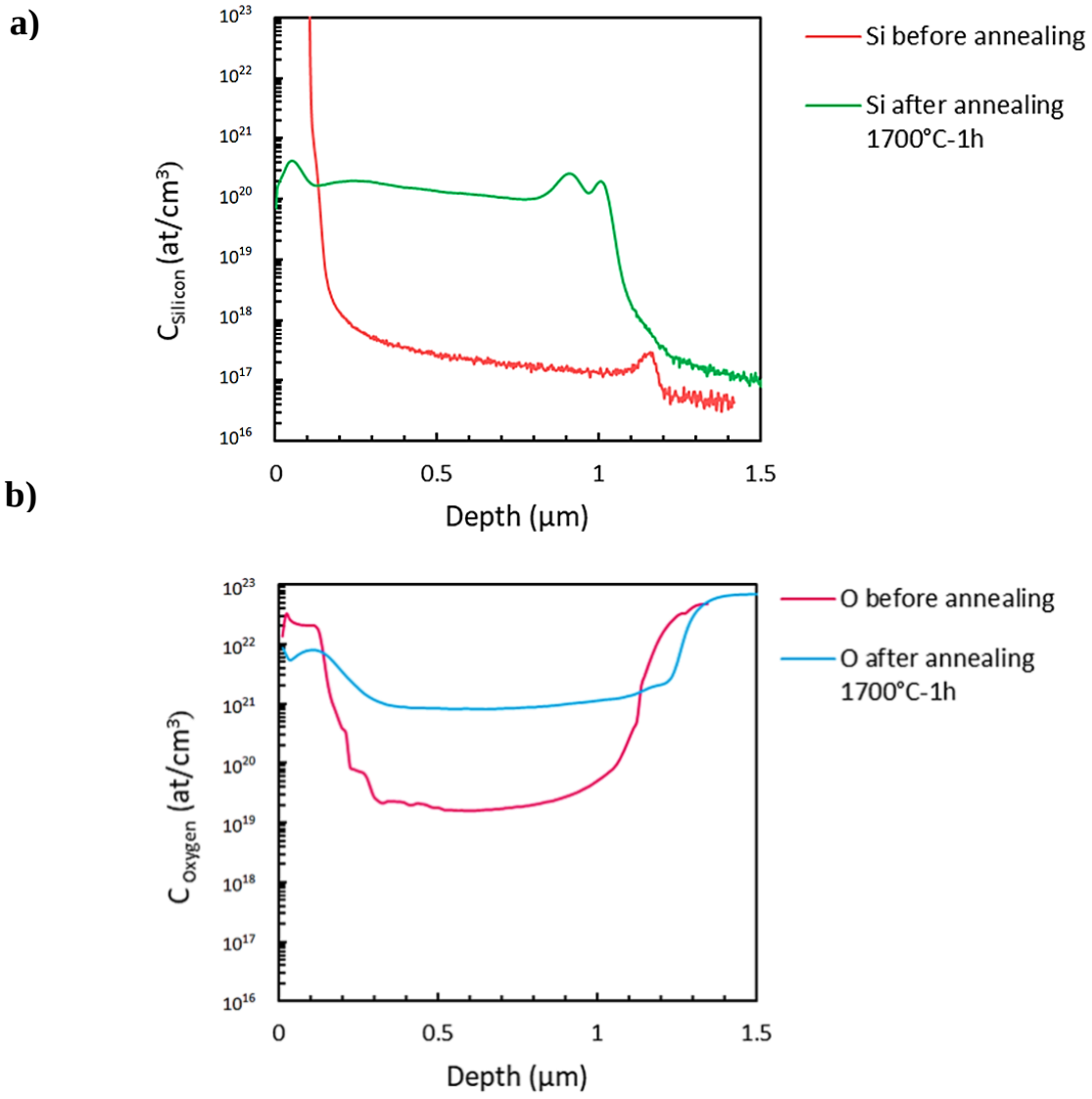

Figure 2: SIMS profiles of **a)** Si in AlN on sapphire with sputtered $Si_{1-x}N_x$ before and after annealing; **b)** O in AlN on sapphire with sputtered $Si_{1-x}N_x$ before and after annealing.

After annealing, the Si depth profile in the AlN shows a plateau at a concentration of 10^{20} at/cm^3, while a value of 10^{17} at/cm^3 is measured in the sample before annealing. Both concentration profiles, before and after annealing, show a slight increase in Si concentration at the AlN/sapphire interface. Corresponding SIMS profiles of O in the AlN layer show an increase in O concentration from 10^{19} at/cm^3 to 10^{21} at/cm^3 after annealing. The concentrations of Si and O resulting from the high temperature annealing are represented by the plateaus of the green and the blue curves, respectively. These concentrations are clearly related to the

diffusion of Si from the sputtered $Si_{1-x}N_x$ layer and O from the sapphire substrate into the epilayer, resulting in co-doping of the AlN.

Fig. 3 shows a cross-sectional HAADF-STEM image along <1-100> projection of the epitaxial AlN after annealing.

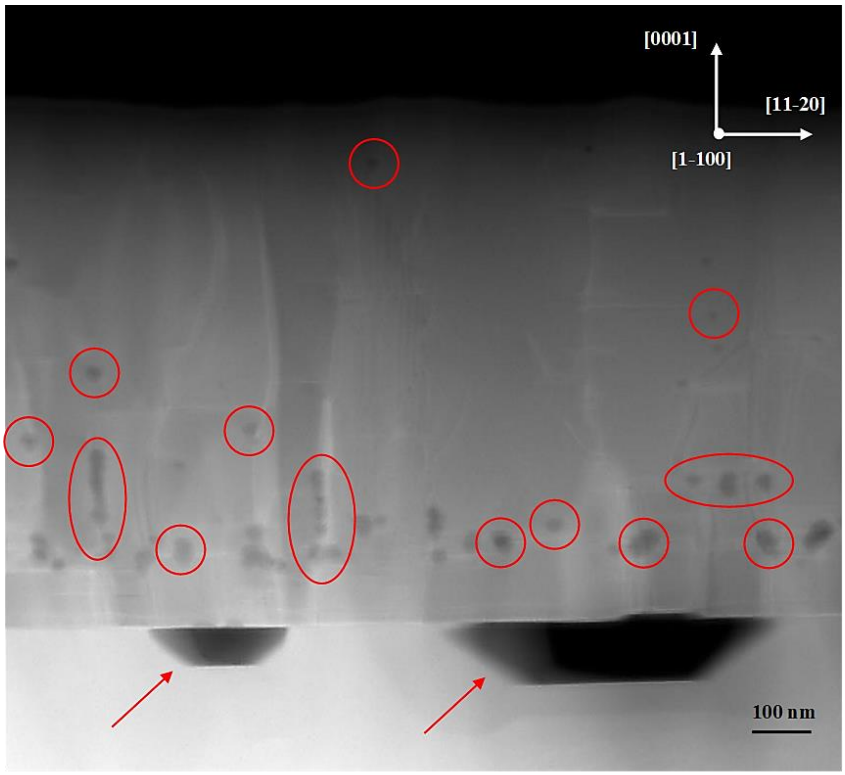

Figure 3: HAADF-STEM in cross-section of epitaxial AlN on sapphire along <1-100> projection of AlN after face to face annealing at 1700°C for 1h. Arrows indicate the voids at the interface between sapphire and AlN. The red circles highlight some of the faceted voids in the AlN epilayer.

The appearance of several dark spots with lower HAADF intensity represents voids appearing in the sample after annealing at high temperature. Fig. 3 shows the presence of voids in both the sapphire substrate and the AlN epilayer. They are highlighted by the red arrows and the red circles, respectively. The voids in the sapphire close to the interface can be explained as the result of the decomposition of sapphire during annealing at high temperature. Studies by Akiyama et al. show that sapphire starts to decompose at around 1200°C in H_2 and NH_3, and around 1400°C under inert atmosphere [40-41]. Regarding the voids

in the AlN epilayer, they have been reported in several studies using high-temperature annealing to achieve defect recovery [42-48].

The phenomenon of void formation in AlN during high temperature annealing has been investigated in detail by Cancellara at al. in similar MOVPE-grown AlN samples [32] and has been shown to be related to the precipitation of vacancies during cool-down.

Fig. 4a provides an overview in cross section of the sample along the <11-20> projection of the AlN epilayer. It shows that defects parallel to the growth plane are created during annealing. These features are homogenously distributed within the entire thickness of the AlN epilayer.

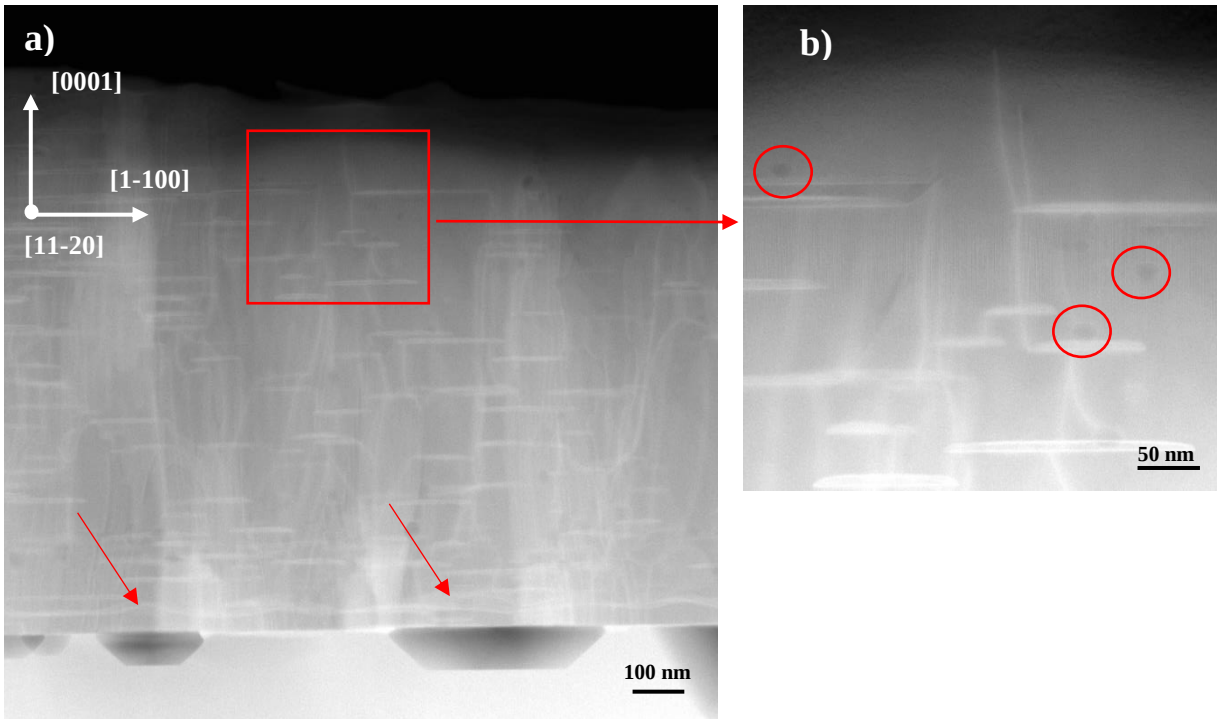

Figure 4*:* **a)** HAADF-STEM in cross-section of epitaxial AlN on sapphire along <11-20> projection of AlN after face to face annealing at 1700°C for 1h. **b)** Magnification of a thin area of the cross section in 4a.

Fig. 4b shows an enlarged view of a thin area of the cross section indicated by the red box in 4a. It highlights that the defects are defined by two boundaries: a lower flat boundary in the growth plane (c-plane) and, on the top of it, a convex dome-

shaped boundary. Their lateral size varies over a wide range that goes from 50 to 300 nm. Their vertical size is only few nanometers.

To analyze the atomic structure of the defects, we study them using high-resolution HAADF-STEM, as shown in fig. 5, where part of one of these defects is analyzed in high resolution along the <11-20> projection of AlN.

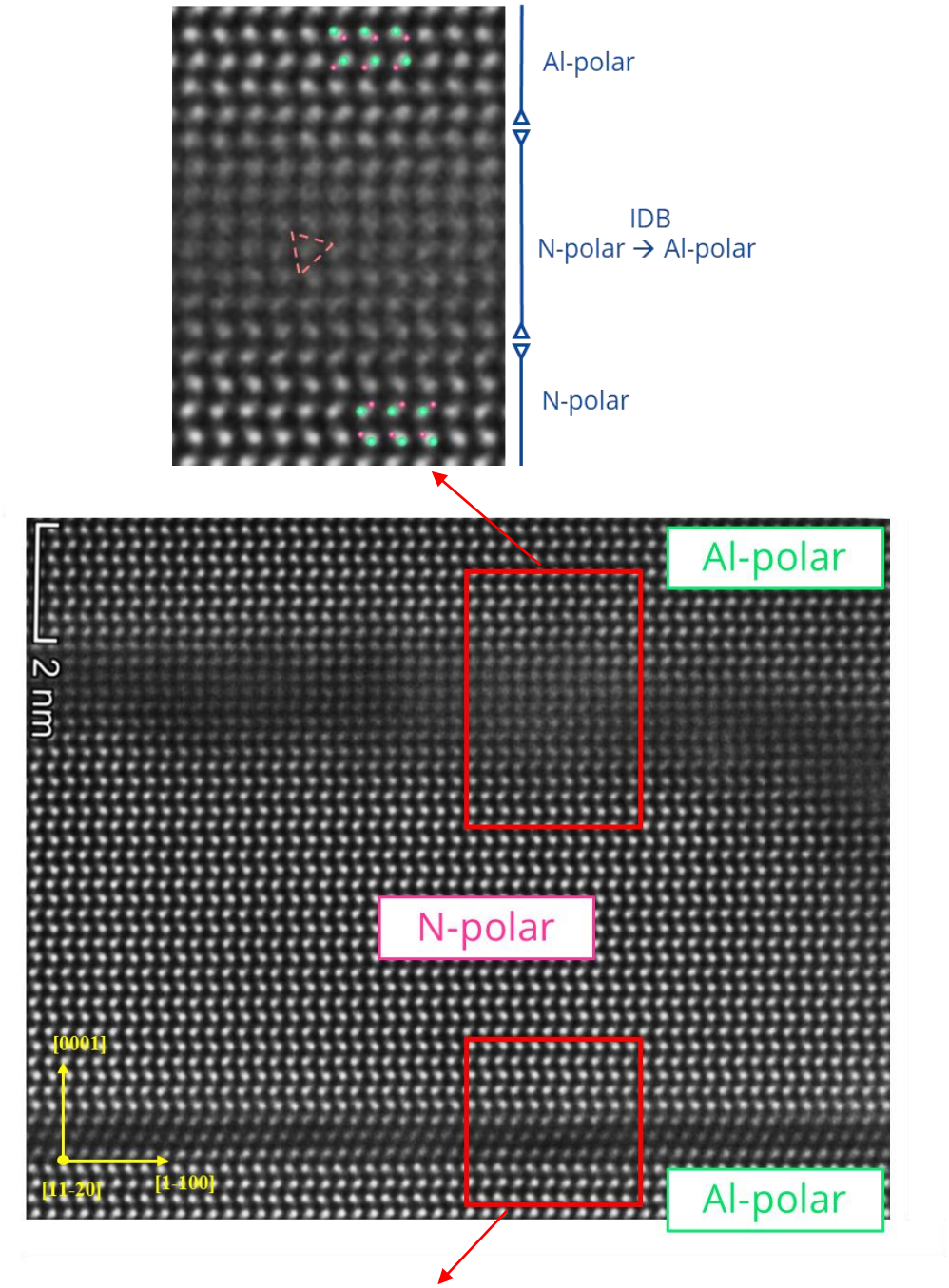

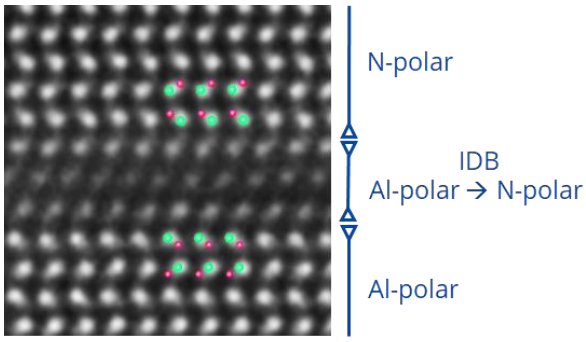

Figure 5: HAADF-STEM in cross section along <11-20> projection of AlN. Representation of the AlN structure is superimposed in the zoomed regions with Al and N atoms in green and pink, respectively, showing inversions of polarity from Al-polar to N-polar and back to Al-polar. The triangle within the upper IDB highlights one of the atomic columns where the contrast does not allow any assignment of polarity.

The intensity in HAADF-STEM images is the result of high-angle electron scattering and provides contrast based on the atomic number of the elements. The brightest contrast spots correspond to the heaviest atoms (Al). In the <11-20> projection of AlN, the intensity is influenced by the distribution of Al and N atoms between the two separated positions of the AlN dumbbell. Thus, it is possible to directly visualize the polarity on the acquired images. Fig. 5 shows that the AlN matrix surrounding the defect is Al-polar, as indicated by the higher intensity of the Al atom occupying the upper position of the AlN dumbbell. This corresponds to the polarity of the as-grown AlN film on sapphire before annealing. On the other hand, the volume inside the defect is N-polar, as indicated by the lower intensity of the N atom in the top position of the AlN dumbbell. The defects emerging in the AlN epilayer after annealing are inversion domains (IDs) and their boundaries appear with reduced intensity compared to the AlN matrix. Following the polarity along the [0001] direction of AlN, the lower flat inversion domain boundary (IDB) switches the Al-polar lattice to N-polar, while the upper IDB switches the N-polar lattice back to metal-polar.

As a comparison, we perform HAADF-STEM in cross section of other two samples, i.e., the epitaxial AlN layer on sapphire without sputtered $Si_{1-x}N_x$ on the surface and the bulk AlN sample with sputtered $Si_{1-x}N_x$, without sapphire

substrate, both annealed at the same experimental conditions (1700°C for 1h in N_2 environment) of the sample previously described. Fig. 6a shows the HAADF-STEM image in cross section of the epitaxial AlN layer on sapphire annealed at high temperature without sputtered $Si_{1-x}N_x$ on the surface. Several faceted voids, indicated by the reduced intensity in the HAADF image, appear in the sample after annealing. Some of these voids are highlighted by the yellow circles in fig. 6a. Furthermore, a continuous bright line close to the interface with the sapphire is detected in the AlN (pointed out by the yellow arrows in fig. 6a. The presence of such a line close to the interface has been already reported by several authors and demonstrated to be an O-rich IDB between a N-polar thin layer and a top Al-polar epilayer [43] [48-49]. Furthermore, Cancellara et al. [32], in their study on crystal recovery of epitaxial AlN, report SIMS profiles of similar samples annealed under the same experimental conditions. They show that, at high temperature (1700°C), O out-diffuses from the sapphire into the AlN layer and reaches a concentration close to 10^{21} cm^{-3}.

Fig. 6b shows a cross-sectional HAADF-STEM micrograph of the bulk AlN sample after annealing at 1700°C for 1 hour with a $Si_{1-x}N_x$ layer deposited on top. In previous studies, a depth diffusion of Si into the bulk AlN of ~1.5 um and a Si concentration of 7.7×10^{19} cm^{-3} [36] is reported for the same sample annealed in the same conditions.

Interestingly, IDs are neither present in the epitaxial AlN on sapphire (fig. 6a) nor in the bulk AlN with $Si_{1-x}N_x$ on top (fig. 6b).

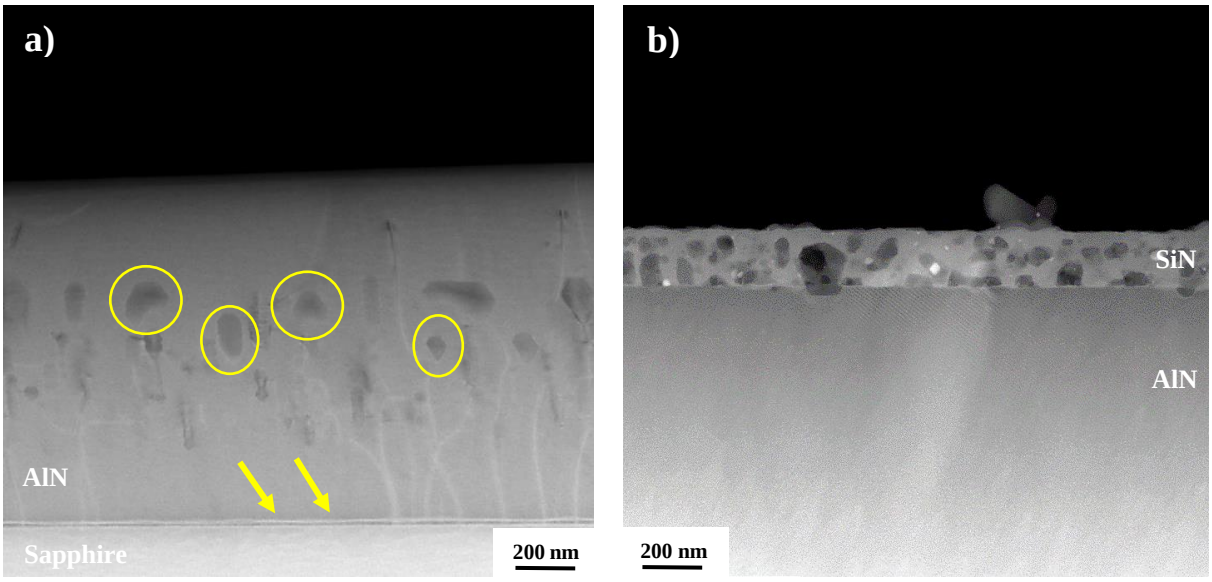

Figure 6: a) Epitaxial AlN on sapphire after annealing at 1700° C for 1h. Yellow circles highlight some of the voids in the AlN epilayer and yellow arrows the planar IDB close to the interface between sapphire and AlN. **b)** Bulk AlN with sputtered $Si_{1-x}N_x$ after annealing at 1700°C for 1h.

Fig. 7 shows EDXS Si-maps together with the correspondent HAADF images in cross section of the AlN epilayer on sapphire with $Si_{1-x}N_x$ deposited on top before and after annealing.

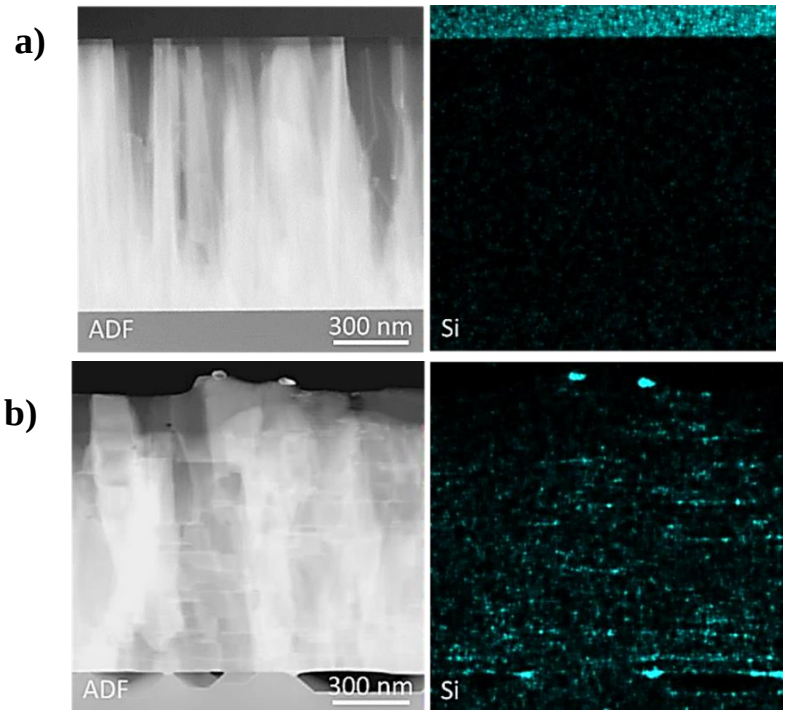

Figure 7: ADF-STEM with the correspondent EDXS Si maps in cross section for the AlN on sapphire with sputtered $Si_{1-x}N_x$ **a)** before annealing and **b)** after annealing.

Before annealing (fig. 7a), Si is confined in the $Si_{1-x}N_x$ top layer and no Si can be detected in the AlN epilayer. After annealing (fig. 7b), Si is detected in the entire thickness of the AlN epilayer. This is consistent with the SIMS profiles reported in fig. 2a. Fig. 7b shows some Si accumulations at the interface AlN/sapphire, in correspondence of the voids, and some residual particles of $Si_{1-x}N_x$ still present on the surface of the epilayer. But more importantly, a noticeable localized increase in Si concentration is detected at the ID sites.

EDX-HAADF investigations at high resolution on a FIB prepared lamella of the same sample in cross section are performed to gain additional insights concerning the chemical characterization of the IDs. Compositional analysis on one of the ID is performed using EDX spectroscopy.

Fig. 8a shows the STEM image of a detail of one of the IDs together with Si, Al, N and O EDX chemical-maps from the orange box crossing the ID. Fig. 8b shows the normalized concentration profiles in atomic percent (at. %) versus distance of Si, Al, N and O for the EDX line scan across the ID represented by the orange arrow in fig. 8a. We find increased concentrations of O and Si at the IDBs, which are accompanied by reduced Al and N contents.

a)

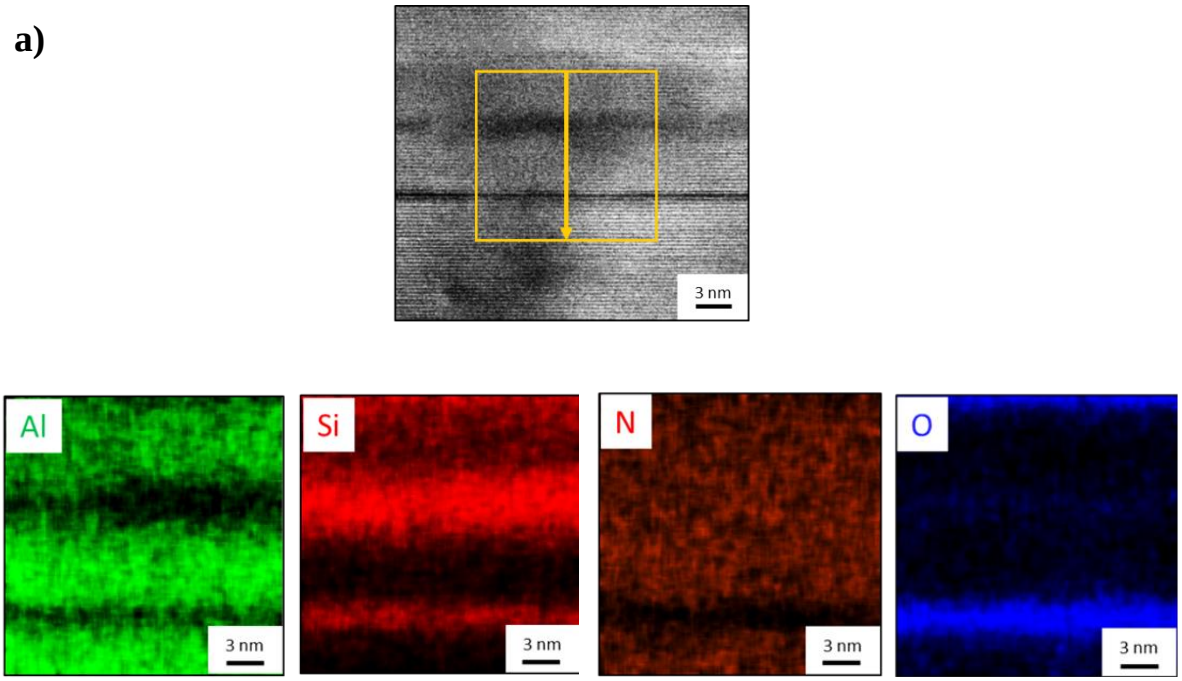

b)

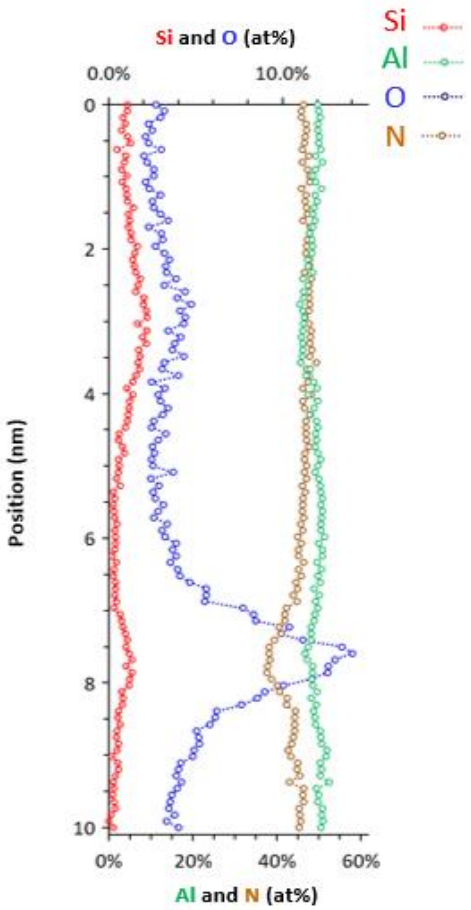

Figure 8: Compositional analysis on one of the ID using quantitative EDX spectroscopy technique. **a)** HAADF-STEM image with EDX chemical-maps crossing the defect (the orange box). **b)** EDX line-scan profile crossing the ID (orange arrow in the orange box in 8a). Normalized concentrations in atomic percentage (at %) of Al, Si, N and O versus distance. Note that the scales for Al, and N and for Si and O are different.

Fig. 9a shows that a small amount of Si (in the range of 0.3 - 1 at%) is detected in the AlN matrix due to bulk diffusion of Si [36]. A small amount of O (in the range of 2.5 - 4 at%) is also present in the AlN matrix due to diffusion of O from the sapphire during annealing [32]. Based on SIMS measurements, assuming a density of 3.26 g/cm^3 and a molar mass of 41 g/mole for AlN, the O and Si contents in AlN were found to be 2 at% and 0.2-0.4 at%, respectively (note that SIMS data for Si vary from 10^{20} to 2×10^{20}). These values are in line with those obtained by EDX.

In fig. 9a, the black data points represent the measured Al+Si and O+N concentrations, while the black solid lines represent the expected concentrations when cations and anions each occupy 50% of the atom sites.

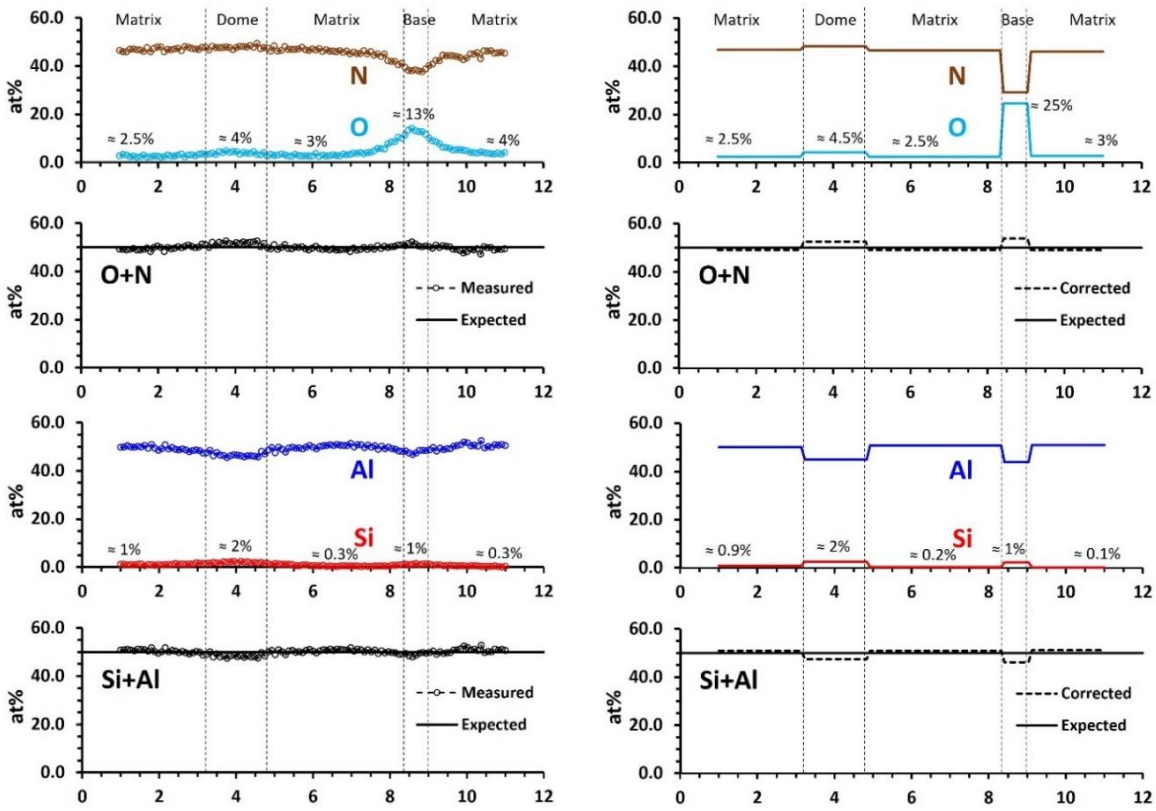

Figure 9: a) Experimental EDX data in atomic percentage (at %) of Al, Si, N and O versus distance. The black data points represent the measured Al+Si and O+N concentrations, while the black solid lines represent the expected concentrations when cations and anions each occupy 50% of the atom sites. **b)** Corrected model for O, N, Si, and Al concentrations, considering beam broadening effect. The dashed black lines represent the corrected concentrations of Al+Si and O+N in comparison with the expected values (black solid lines).

The EDXS results on the IDs shown in fig. 9 reveal significant differences in chemical composition at the IDBs compared to the surrounding matrix, with enrichments of O and Si and reductions in Al and N concentrations. For a comprehensive analysis of EDXS on the FIB lamellae, the IZAC code [50] plays a crucial role enabling a more accurate and precise evaluation of the results. The IZAC code calculates the lamella thickness, the absorption in the various layers and the channeling using standards of known thickness and composition. Given the lamella thickness of 280 nm, an additional correction for beam broadening is required. This is achieved by applying a correction model to the measured values. Based on the HAADF-STEM results shown in fig. 5, we assume a thickness of 0.7 nm for the lower IDB (labeled as base in fig. 9) and 1.7 nm for the upper IDB (labeled as dome in fig. 9). The model calculates the concentration of O, N, Si and Al to fit the measured concentration profiles. The corrected results are shown in fig. 9b, confirming the replacement of N by O, and the replacement of Al by Si.
It should be noted that the chemical composition analysis of the upper IDB is considered less reliable due to dome-like shape, resulting in the convolution of the EDX spectra with both the matrix and the IDB in the projection direction.

Discussion

This study focuses on the analysis of the IDs observed in the epitaxial AlN layer on sapphire with $Si_{1-x}N_x$ deposited on top after annealing at 1700°C for 1 h. These IDs are characterized by two IDBs: a flat IDB that inverts the polarity from Al-polar to N-polar (base IDB) and a dome-shaped IDB that reverts the polarity from N-polar back to Al-polar (dome IDB).
Prior studies demonstrated that the formation of an octahedral monolayer with the metal in the center being surrounded by O/N produces polarity inversions from Al-polar to N-polar in AlN [29] [52-53]. To analyze the flat IDB where the polarity changes from Al-polar to N-polar, we refer to the aluminum-oxynitride

system ($Al_xO_3N_{x-2}$), particularly to $Al_9O_3N_7$-27R [54-57], whose atomic structure is reported in fig. 10.

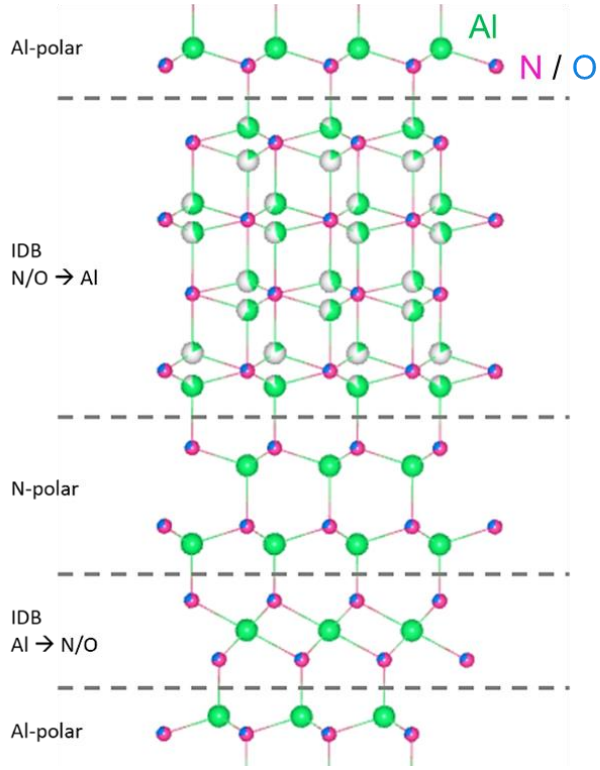

Figure 10: Ball-and-stick representation of $Al_9O_3N_7$-27R structure. The tetrahedral sites are occupied by Al-cations and the anion positions are shared between N- and O-atoms. Within the N/O→Al IDB, the tetrahedral sites are partially filled. Characteristic for the Al→N/O-IDB is the octahedral coordination of the Al-atoms.

The atomic structure of $Al_9O_3N_7$-27R is based on the crystal structure of wurtzite AlN with different polarities and two distinct inversion domains boundaries (IDBs). One IDB changes the lattice from metal to non-metal-polarity and spans over one monolayer, with Al-atoms arranged in an octahedral coordination. The stacking of the lattice changes by a $\frac{a}{3} < 1\bar{1}00 >$ basal plane translation. The counterpart IDB reverses the non-metal-polar lattice back to metal-polar and covers several monolayers. Within this latter IDB, anions form a hexagonal closed-packed structure, where the tetrahedral sites are partially filled by cations (Al-atoms), with cations in the up-pointing tetrahedra being metal-polar and those in down-pointing tetrahedra being non-metal-polar. The occupancy of cations in

these positions is complementary, adding up to 100%, but their distribution varies with the position within the structure along the <0001> direction. The occupancy at non-metal-polar sites gradually decreases, while the number of cations on the metal-polar positions increases.

Fig. 11 shows a HRTEM image of a portion of one of the flat IDBs in our sample. We use imaging conditions with a small negative C_s value and a positive defocus [38-39] [58] for obtaining optimal contrast in HRTEM. In these conditions, atomic resolution is achieved even for lighter elements. The polarity changes from Al-polar to N-polar with a discontinuity in the stacking sequence and contains a lateral in-plane displacement. The stacking of the atomic layers along the c-direction can be described as A-B-A-B-C-B-C (fig. 11b), where A, B, C are the stacking positions along the c-axis.

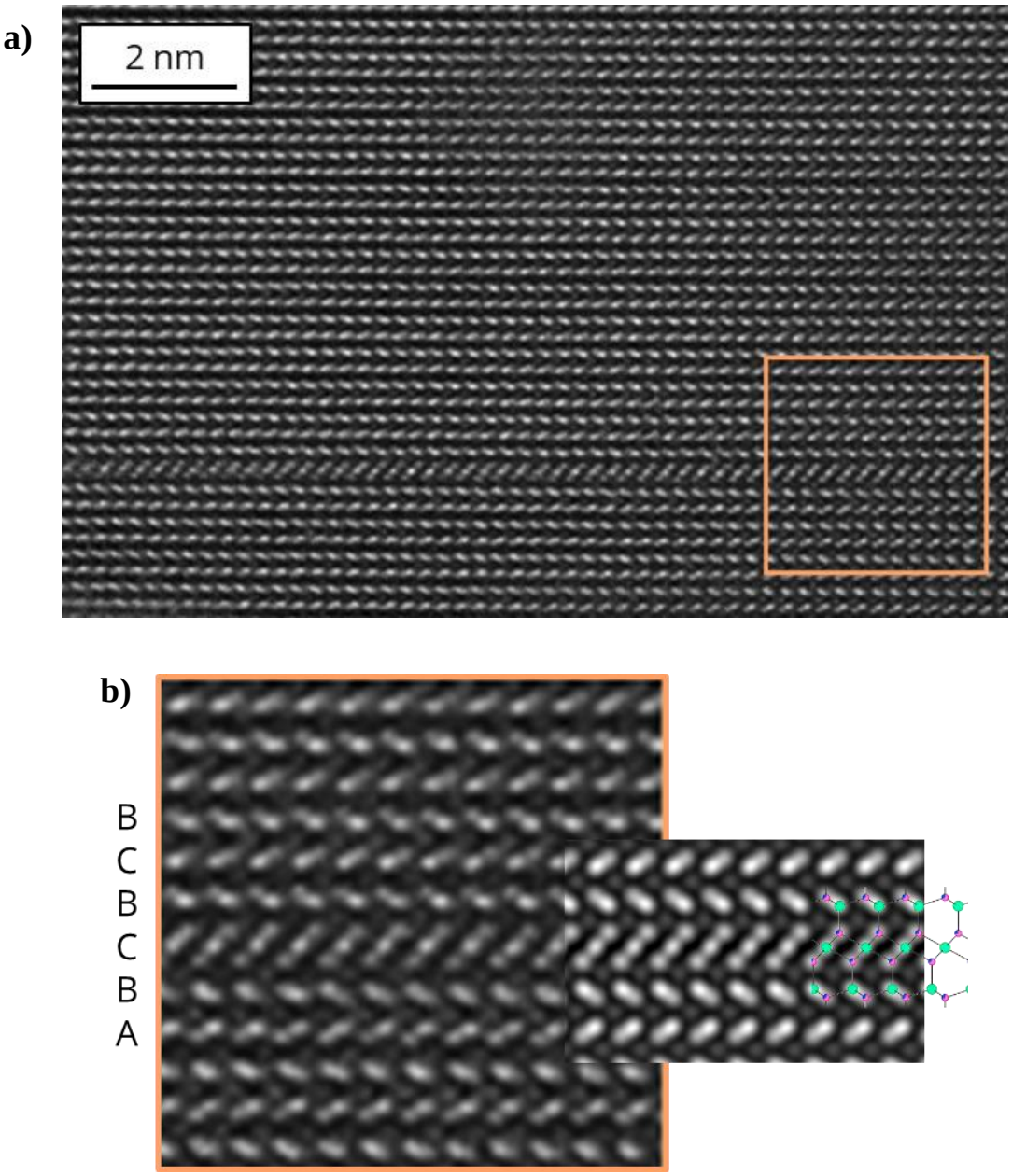

Figure 11: a) HRTEM image along the <11-20> projection, showing the IDB between Al-polar and N-polar. **b)** Magnification of the area in the orange square in 10a. The experimental HRTEM image is compared to the phase contrast simulation of the IDB in $Al_9O_3N_7$-27R for a sample thickness of 4 nm. The theoretical stick-and-ball structure is overlapped to the microstructure. The anion positions are shared between N (purple) and O (blue) atoms. The cation positions are occupied by Al/Si (green).

We compare our experimental HRTEM image along the <11-20> projection of AlN with the simulation of the HRTEM pattern for the IDB from Al-polar to N-polar in $Al_9O_3N_7$-27R. We use simulation parameters corresponding to our experimental conditions: an acceleration voltage of 300 kV, a semi-convergence angle of 0.3 mrad, a defocus spread of 2.9 nm, a spherical aberration C_S = -12 µm

and a slight over-focus of 5 nm. The simulation image reported in fig. 11b is obtained for a sample thickness of 4 nm. In the considered structure (as for $Al_9O_3N_7$-27R), Al atoms are octahedrally coordinated and the stacking of the lattice changes by a $\frac{a}{3} < 1\bar{1}00 >$ basal plane translation (along the c-direction). In fig. 11b we show excellent agreement between the experimental HRTEM image and the simulated phase contrast image. The corresponding theoretical stick-and-ball structure of $Al_9O_3N_7$-27R is overlapped to the simulated structure in fig. 11b.

Several research groups have extensively studied polarity inversions from N-polar to metal-polar during growth of AlN [9-10] [18] [51]. It has been demonstrated that the presence of O during growth plays an essential role in this polarity transformation [19-21]. The IDB from N-polar to Al-polar can be described as two interpenetrating sublattices: a non-metal-polar wurtzite lattice and a metal-polar wurtzite lattice that share a common anion sublattice. All arising tetrahedral sites are partially filled by cations, but the inner distribution depends on the position within the structure. Along <0001>, the cation occupancy of the N-polar sub-lattice gradually decreases, while the cation occupancy on the metal-polar sublattice increases [19-21]. The high-resolution HAADF-STEM image (fig. 5) shows a triangular (or roundish) contrast within the upper IDB, which does not allow any assignment of polarity, indicating that the cation is shifted towards lower or upper positions (corresponding to N- or Al-polar sub-lattices, respectively). The reduced intensity in the HAADF-STEM image is caused by the reduced effective atomic number of the Al columns, due to the statistical distribution of Al atoms between the cation sites of Al-polar and N-polar sub-lattices [19-21].

Fig. 9 shows a comparison between the expected concentrations of Al+Si and O+N (black solid lines in fig. 9a and 9b) when cations and anions each occupy 50% of the atom sites with the measured and corrected concentrations of Al+Si and O+N (black data series in fig. 9a and black dashed lines in fig. 9b,

respectively). Both IDBs exhibit a slight excess of O+N and a deficit of Si+Al in both the measured and corrected profiles. This observation aligns with the existence of an additional anion monolayer in the lower IDB, partially occupied by O, as illustrated in the theoretical stick-and-ball structure of $Al_9O_3N_7$-27R. In the proposed model, the environment of Al (Si) cations changes from tetrahedral, where each cation is linked to 4 O(N) anions, to octahedral, where each cation is linked to 6 O(N) anions. This change can explain the observed increase in the [O+N]/[Al+Si] ratio.

The formation of such IDs is not observed under conditions with comparable O or Si concentrations alone (as shown in fig. 6) [32] [36]. Consequently, we can conclude that the presence of O, in conjunction with Si, is a requisite for the formation and stabilization of these IDs.

Previous studies on diffusion of Si [36] and O [32] in AlN have revealed that the incorporation of Si results in the substitution of Al atoms at cation sites (Si_{Al}), while the incorporation of O leads to the substitution of N atoms at anion sites (O_N). These substitution processes are accompanied by the formation of vacancies (V_{Al} and V_N) within the crystal structure [32] [36] [58], with a clear correlation between the presence of impurities/vacancies and the phenomenon of polarity inversion in AlN [24]. At the high temperature used during annealing, the solubilities of Si_{Al} and O_N impurities are higher than at room temperature. During the cool-down phase, the excess of Si and O precipitates in the crystal. This precipitation of impurities is facilitated by V_{Al} and V_N, which ultimately play an important role in promoting the formation of the IDs. Here we describe a mechanism for the formation of the closed IDs through the precipitation of Si and O in the basal c-plane during the cooling process.

A. D. Westwood et al., in their study on AlN powders containing O, proposed a formation mechanism for both planar and curved IDBs [29]. This mechanism is shown in details in fig. 12 and consists of three main steps:

- First, due to supersaturation of O in the AlN, octahedral clusters precipitate on the basal plane and cause the formation of O-rich platelets (fig. 12a). This arrangement leaves a plane of Al atoms in unfavorable positions. These atoms carry a net charge and the structure is not electrically neutral.
- In the second step, to achieve electrical neutrality and stability, a simple translation is performed by those Al atoms, creating a planar inversion of polarity (fig. 12b).
- In the final step, as a direct consequence of the stabilization mechanism of the planar IDB, a curved IDB is generated at the intersection between the translated Al atoms and the Al sublattice of the matrix that has not undergone translation (fig. 12c). This curved IDB forms as a result of non-stoichiometry within the crystal and its morphology derives from local changes in the chemical composition in proximity to the planar IDB.

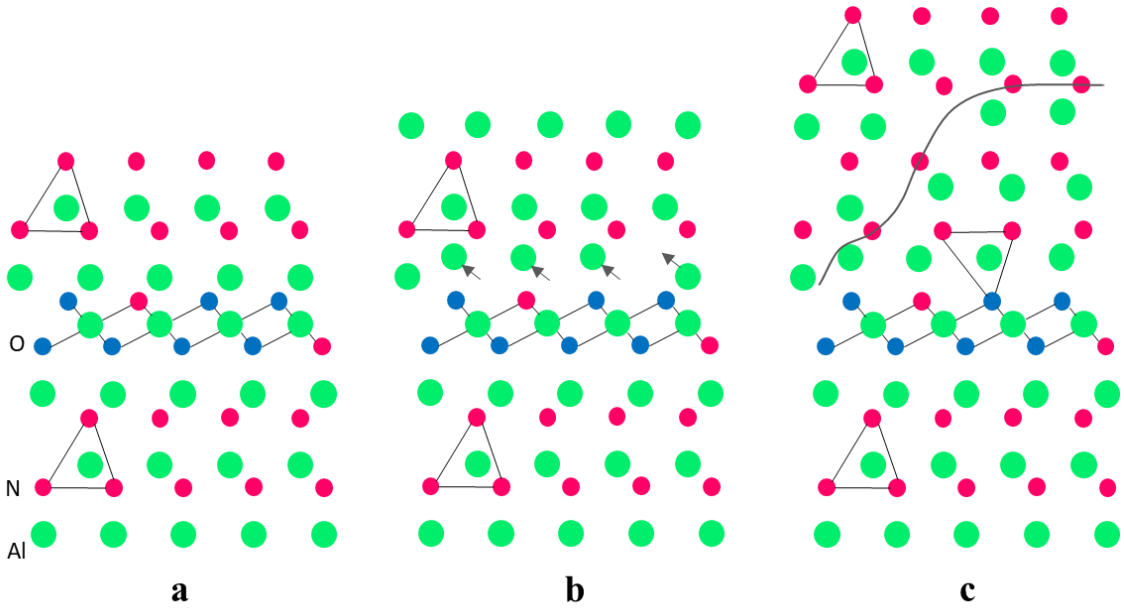

Figure 12: Representation of the formation mechanism for the planar and curved IDBs in the A1N structure according to Westwood´s model [29]. The green circles represent Al-atoms, the magenta circles are N-atoms, and the blue circles are O-atoms. **a)** Precipitation of octahedral clusters on the basal plane. This creates two adjacent stacking faults, leaving a plane of Al atoms in unfavorable sites. **b)** Translation of those Al atoms from one tetrahedral site to the opposite tetrahedral site. This creates an inversion across the planar IDB and produces an electrically neutral interface. **c)** Creation of the curved IDB as a direct consequence of the translation in b). The inversion domain formed by the translation of the Al atoms produces a second IDB (curved) at the point where Al atoms which have been translated meet with the Al sublattice which has not been translated.

The mechanism proposed by Westwood et al. for AlN powders can be well applied to the formation of the IDs reported in our study, with the difference that, in the case of AlN powders, high concentration of O is sufficient to create these IDs, while, in the case of the epitaxial AlN described in our study, co-doping with Si and O is shown to be essential.

Why could the presence of Si promote polarity inversions in epitaxial AlN? Youngman and Harris reported that defect clusters of [V_{Al}+O_N] can be formed by small additions of O [24] [59-60], but these clusters have relatively low effect on the stability of the wurtzite structure of AlN (i.e. they do not lead to polarity inversions). However, higher O concentrations increase the density of [V_{Al}+O_N] defect clusters until a critical point is reached, where the Al coordination goes from tetrahedral to octahedral. As proposed in the model by Westwood, these octahedral clusters represent the starting structural units for the formation of the IDBs. In the case of AlN powders, grain boundaries act as high diffusion paths, leading to rapid diffusion of O into AlN and high concentration of [V_{Al}+O_N] clusters. While in the case of epitaxial AlN, O diffusion is slower as [V_{Al}+O_N] clusters are present in lower concentration, and this has only a small effect on the stability of the AlN crystal structure. In this context, the presence of Si impurities might play a crucial role in enhancing the diffusion and clustering of point defects, in particular V_N, thereby facilitating the precipitation of O in the bulk material, enabling formation/stabilization of the IDs and reestablishing electrical neutrality. A supporting observation is that, in similar samples annealed under identical conditions by Cancellara et al. [32], the O concentration detected by SIMS is lower than in our sample. In their study, the presence of voids in AlN after annealing indicated clustering of vacancies, but the insufficient O concentration prevented the formation of IDBs. On the other hand, our findings highlight that the presence of V_N, facilitated by Si, allows reaching the critical O concentration necessary for the formation of IDBs. Ultimately, the high concentration of

impurity-vacancy clusters in the AlN might affect the stability of the crystal structure, promoting the transformation of the cation coordination from tetrahedral to octahedral and, subsequently, giving rise to the IDBs, as described by Westwood.

Interestingly, impurities have also been reported to influence the formation of IDs in other III-nitride materials. For instance, the introduction of high Mg-doping in epitaxial GaN has been associated with the formation of pyramidal-shaped domains with reversed polarity compared to the surrounding material [24-26]. The exact mechanism responsible for the formation of these pyramidal IDs remains a subject of ongoing investigation. Nevertheless, a hint arises from the observation that their size is affected by the growth temperature of the GaN epilayers. These pyramidal IDs become larger as the growth temperature increases [61]. This observation implies that diffusion processes may be involved in their creation and, similarly to what we have observed in our AlN samples, their formation mechanism may be related to precipitation of impurities during cooling down from the growth temperature.

Conclusions

This study contributes to a growing body of research that emphasizes the importance of impurities in polarity control within III-nitride materials. We have investigated the effect of Si and O co-doping in epitaxial AlN on sapphire with $Si_{1-x}N_x$ deposited on the top surface, following high-temperature annealing. One of the key findings is the identification of polarity IDs occurring post-growth, during the annealing process, showing Si and O enrichments in correspondence of their boundaries. This indicates that the diffusion of Si and O during annealing plays a crucial role in the formation/stabilization of the IDs and emphasizes the influence of impurities on the polarity inversion mechanism.

The formation of polarity inversions and the role of impurity-vacancy clusters in their development offer valuable insights for the engineering of advanced

electronic and optoelectronic applications based on polarity manipulation. Co-doping with Si and O holds promising potential for advancing the evolution of high-performance devices featuring alternating polarities, such as film bulk acoustic wave resonators [6] and quasi-phase matching non-linear optics devices [62-63].

Bibliography

[1] T. Takeuchi, C.Wetzel, S. Yamaguchi, H. Sakai, H. Amano, I. Akasaki, Y. Kaneko, S. Nakagawa, Y. Yamaoka, and N. Yamada, Appl. Phys. Lett. 73, 1691 (1998).

[2] M. Leroux, N. Grandjean, M. Laügt, J. Massies, B. Gil, P. Lefebvre, and P. Bigenwald, Phys. Rev. B 58, R13371 (1998).

[3] T. K. Zywietz, J. J. Neugebauer, and M. Scheffler, Appl. Phys. Lett. 74, 1695–1697 (1999).

[4] N. A. Fichtenbaum, T. E. Mates, S. Keller, S. P. DenBaars, and U. K. Mishra, J. Cryst. Growth 310, 1124–1131 (2008).

[5] O. Ambacher, J. Appl. Phys. 85, 3222 (1999).

[6] A. Chowdhury, H. M. Ng, M. Bhardwaj, and N.G.Weimann, Appl. Phys. Lett. 83, 1077 (2003).

[7] J. Park, Y. Yamazaki, M. Iwanaga, S. Ahn, H. Jeon, T. Fujiwara, and T. Yao, Opt. Express 18, 7851 (2010).

[8] K. Hestroffer, C. Leclere, C. Bougerol, H. Renevier, and B. Daudin, Phys. Rev. B 84, 245302 (2011).

[9] H. Amano, N. Sawaki, I. Akasaki, and Y. Toyoda, Appl. Phys. Lett. 48, 353 (1986).

[10] S. Nakamura, Jpn. J. Appl. Phys. 30, L1705 (1991).

[11] Y. Chen, S.-K. Hong, H.-J. Ko, V. Kirshner, H. Wenisch, T. Yao, K. Inaba, and Y. Segawa, Appl. Phys. Lett. 78, 3352 (2001).

[12] Y. Chen, H.-J. Ko, S.-K. Hong, and T. Yao, Appl. Phys. Lett. 76, 559 (2000).

[13] L. Romano, J. Northrup, A. Ptak, and T. Myers, Appl. Phys. Lett. 77, 2479 (2000).

[14] N. Grandjean, M. L. Talent, A. Dussaigne, P. Vennéguès, and E. Tournié, MBE 2002 - 2002 12th International Conference on Molecular Beam Epitaxy 251, 141–142 (2002).

[15] P. Vennéguès, P. Vennéguès, M. Leroux, S. Dalmasso, M. Benaissa, P. De Mierry, P. Lorenzini, B. Damilano, B. Beaumont, J. Massies, and P. Gibart, Phys. Rev. B 68 (2003).

[16] S. Pezzagna, P. Vennéguès, N. Grandjean, and J. Massies, J. Cryst. Growth 269, 249–256 (2004).

[17] H. Kawakami, K. Sakurai, K. Tsubouchi, and N. Mikoshiba, Jpn. J. Appl. Phys. 27, L161 (1988).

[18] J. L. Rouvière, M. Arlery, R. Niebuhr, K. H. Bachem, and O. Briot, Mater. Sci. Eng. B 43, 161 (1997).

[19] S. Mohn, N. Stolyarchuk, T. Markurt, R. Kirste, M. P. Hoffmann, R. Collazo, A. Courville, R. Di Felice, Z. Sitar, P. Vennéguès, and M. Albrecht, Phys. Rev. Applied 5, 054004 (2016)

[20] N. Stolyarchuk, T. Markurt, A. Courville, K. March, O. Tottereau, P. Vennéguès, and M. Albrecht, J. Appl. Phys. 122, 155303 (2017).

[21] N. Stolyarchuk, T. Markurt, A. Courville, K. March, J. Zúñiga-Pérez, P. Vennéguès, and M. Albrecht, Sci Rep 8, 14111 (2018).

[22] M. Akiyama, T. Kamohara, K. Kano, A. Teshigahara, and N. Kawahara, Appl. Phys. Lett. 93, 021903 (2008). https://doi.org/10.1063/1.2957654

[23] T. Mizuno, K. Umeda, Y. Aida, A. Honda, M. Akiyama, T. Nagase, and M. Kobayashi, in 2017 19th International Conference on Solid-State Sensors, Actuators and Microsystems (TRANSDUCERS). 1891-1894.

[24] S. A. Anggraini, M. Uehara, K. Hirata, H. Yamada and M. Akiyama, Sci Rep 10, 4369 (2020). https://doi.org/10.1038/s41598-020-61285-8

[25] P. Vennéguès, M. Benaissa, B. Beaumont, E. Feltin, P. De Mierry, S. Dalmasso, M. Leroux, and P. Gibart, Appl. Phys. Lett. 77, 880–882 (2000). https://doi.org/10.1063/1.1306421

[26] Z. Liliental-Weber, M. Benamara, J. Washburn, I. Grzegory, and S. Porowski, Phys. Rev. Lett. 83, 2370-2373 (1999). https://doi.org/10.1103/PhysRevLett.83.2370

[27] J. Mater. Res., Vol. 10, No. 5, May 1995.
[28] J. H. Harris, R. A. Youngman, and R. G. Teller, J. Mater. Res. 5, 1763-1773 (1990).
[29] A. D. Westwood, R. A. Youngman, M. R. McCartney, A. N. Cormack, and M.R. Notis, J. Mater. Res. 10, 1287-1300 (1995).
[30] H. Li, T. C. Sadler, and P. J. Parbrook, "AlN heteroepitaxy on sapphire by metalorganic vapour phase epitaxy using low temperature nucleation layers," Journal of Crystal Growth 383, 72–78 (2013).
[31] S. Hagedorn, A. Mogilatenko, S. Walde, D. Pacak, J. Weinrich, High-Temperature Annealing and Patterned AlN/Sapphire Interfaces. Phys. Status Solidi B 2021,258, 2100187
[32] L. Cancellara, T. Markurt, T. Schulz, M. Albrecht, S. Hagedorn, S. Walde, M. Weyers, S. Washiyama, R. Collazo and Z. Sitar. Role of oxygen diffusion in the dislocation reduction of epitaxial AlN on sapphire during high-temperature annealing. J. Appl. Phys. 130, 203101 (2021).
[33] C. Hartmann, J. Wollweber, A. Dittmar, K. Irmscher, A. Kwasniewski, F. Langhans, T. Neugut and M. Bickermann, Jpn. J. Appl. Phys. 52, 08JA06 (2013).
[34] C. Hartmann, A. Dittmar, J. Wollweber, and M. Bickermann, Semiconductor Science and Technology 29 (8), 084002 (2014)
[35] X. F. Chen, D. Siche, M. Albrecht, C. Hartmann, J. Wollweber and X. G. Xu, Crystal Research and Technology 43 (6), 651-655 (2008).
[36] V. Bonito Oliva, D. Mangelinck, S. Hagedorn, H. Bracht, K. Irmscher, C. Hartmann, P. Vennéguès, and M. Albrecht, J. Appl. Phys. 134, 095103 (2023). https://doi.org/10.1063/5.0159641
[37] S. Brotzmann, and H. Bracht, J. Appl. Phys. 103, 033508 (2008). https://doi.org/10.1063/1.2837103
[38] C. L. Jia, and K. Urban, Science 303, 2001-2004 (2004). https://doi.org/10.1126/science.1093617

[39] M. de la Mata, C. Magen, J. Gazquez, M. I. B. Utama, M. Heiss, S. Lopatin, F. Furtmayr, C. J. Fernández-Rojas, B. Peng, J. R. Morante, R. Rurali, M. Eickhoff, A. Fontcuberta i Morral, Q. Xiong, and J. Arbiol, Nano Lett., 12, 2579−2586 (2012). https://doi.org/10.1021/nl300840q

[40] K. Akiyama, T. Araki, H. Murakami, Y. Kumagai, and A. Koukitu, Phys. Status Solidi Curr. Top. Solid State Phys., vol. 4, no. 7, pp. 2297–2300 (2007). https://doi.org/10.1002/pssc.200674816

[41] K. Akiyama, Y. Ishii, H. Murakami, Y. Kumagai, and A. Koukitu, J. Cryst. Growth, vol. 311, no. 10, pp. 3110–3113 (2009). https://doi.org/10.1016/j.jcrysgro.2009.01.079

[42] S. Washiyama, Y. Guan, S. Mita, R. Collazo, and Zlatko Sitar, J. Appl. Phys. 127, 115301 (2020). https://doi.org/10.1063/5.0002891

[43] H. Miyake, C. H. Lin, K. Tokoro, and K. Hiramatsu, J. Cryst. Growth, vol. 456, pp. 155–159 (2016). https://doi.org/10.1016/j.jcrysgro.2016.08.028

[44] L. Cancellara, S. Hagedorn, S. Walde, D. Jaeger, and M. Albrecht, J. Appl. Phys. 131, 215304 (2022). https://doi.org/10.1063/5.0088948

[45] J. Ben, Z. Shi, H. Zang, X. Sun, X. Liu, W. Lü, and D. Li, Appl. Phys. Lett. 116, 251601 (2020). https://doi.org/10.1063/5.0012792

[46] S. Xiao, R. Suzuki, H. Miyake, S. Harada, and T. Ujihara, J. Cryst. Growth, vol. 502, pp. 41–44, (2018). https://doi.org/10.1016/j.jcrysgro.2018.09.002

[47] J. Ben, X. Sun, Y. Jia, K. Jiang, Z. Shi, H. Liu, Y. Wang, C. Kai, Y. Wu, and D. Li, CrystEngComm, vol. 20, no. 32, pp. 4623–4629 (2018). https://doi.org/10.1039/c8ce00770e

[48] K. Shojiki, K. Uesugi, S. Kuboya, T. Inamori, S. Kawabata, and H. Miyake, Phys. Status Solidi B 2021, 258, 2000352 (2020). https://doi.org/10.1002/pssb.202000352

[49] T. Akiyma, M. Uchino, K. Nakamura, T. Ito, S. Xiao, H. Miyake, Jpn. J. Appl. Phys. 58, SCCB30 (2019). https://doi.org/10.7567/1347-4065/ab0d01

[50] E. Robin, US patent (2016) 0169668 A1.

[51] H. Kawakami, K. Sakurai, K. Tsubouchi, and N. Mikoshiba, Jpn. J. Appl. Phys. 27, L161 (1988). https://doi.org/10.1143/JJAP.27.L161

[52] Y. Yan, M. Terauchi, and M. Tanaka, Philosophical Magazine A, 77:4, 1027-1040 (1998). https://doi.org/10.1080/01418619808221226

[53] R. Youngman, A. Westwood, and M. McCartney, MRS Online Proceedings Library 319, 45–50 (1993). https://doi.org/10.1557/PROC-319-45

[54] T. Asaka, H. Banno, S. Funahashi, N. Hirosaki, and K. Fukuda, Journal of Solid-State Chemistry, 204, 21–26 (2013). https://doi.org/10.1016/j.jssc.2013.05.007

[55] T. Asaka, T. Kudo, H. Banno, S. Funahashi, N. Hirosaki, and K. Fukuda, Powder Diffraction, 28(03), 171–177 (2013). https://doi.org/10.1017/s0885715613000419

[56] K. H. Jack, J Mater Sci 11, 1135–1158 (1976). https://doi.org/10.1007/BF00553123

[57] J. McCauley, P. Patel, M. Chen, G. Gilde, E. Strassburger, B. Paliwal, K. T. Ramesh, and D. Dandekar, Journal of the European Ceramic Society, 29, 223-236 (2009). https://doi.org/10.1016/j.jeurceramsoc.2008.03.046

[58] Q. Yan, A. Janotti, M. Scheffler, and C. G. Van de Walle, Appl. Phys. Lett. 105, 111104 (2014). https://doi.org/10.1063/1.4895786

[59] A. D. Westwood, R. A. Youngman, M. R. McCartney, A. N. Cormack, and M. R. Notis, J. Mater. Res. 10, 1270-1286 (1995).

[60] R. A. Youngman, and J. H. Harris, Journal of the American Ceramic Society 73, 3238-3246 (1990). https://doi.org/10.1111/j.1151-2916.1990.tb06444.x

[61] P. Vennéguès, et al., unpublished work.

[62] S. Pezzagna, P. Vennéguès, N. Grandjean, A. D. Wieck, and J. Massies, Appl. Phys. Lett. 87, 062106 (2005). https://doi.org/10.1063/1.2009839

[63] M. Suzuki, T. Yanagitani, and H. Odagawa, Appl. Phys. Lett. 104, 172905 (2014). https://doi.org/10.1063/1.4874840